Estimation of the bed shear stress in vegetated and bare channels with smooth beds

Estimation of the bed shear stress in vegetated and bare channels with smooth beds

Judy Q. Yang,[1] Francois Kerger,[1] Heidi M. Nepf[1]

Corresponding author: Judy Qingjun Yang, Department of Civil and Environmental Engineering, Massachusetts Institute of Technology, 15 Vassar Street, Building 48-216D, Cambridge, MA 02139, USA. (qjyang@mit.edu)

[1]Department of Civil and Environmental Engineering, Massachusetts Institute of Technology, Cambridge, Massachusetts, USA

Abstract. The shear stress at the bed of a channel influences important benthic processes such as sediment transport. Several methods exist to estimate the bed shear stress in bare channels without vegetation, but most of these are not appropriate for vegetated channels due to the impact of vegetation on the velocity profile and turbulence production. This study proposes a new model to estimate the bed shear stress in both vegetated and bare channels with smooth beds. The model, which is supported by measurements, indicates that for both bare and vegetated channels with smooth beds, within a viscous sub-layer at the bed, the viscous stress decreases linearly with increasing distance from the bed, resulting in a parabolic velocity profile at the bed. For bare channels, the model describes the velocity profile in the overlap region of the Law of the Wall. For emergent canopies of sufficient density (frontal area per unit canopy volume $a \geq 4.3m^{-1}$), the thickness of the linear-stress layer is set by the stem diameter, leading to a simple estimate for bed shear stress.

1. Introduction

In aquatic systems, sediment transport plays a significant role in the function and morphology of hydraulic structures [*Robbins and Simon*, 1983; *Bennett et al.*, 2008; *García*, 2008], the erosion and geomorphic evolution of coastal areas and channels [*Christiansen et al.*, 1981; *Shields et al.*, 1995; *Gacia and Duarte*, 2001; *Shields Jr et al.*, 2004], the turbidity of fish habitats [*Lenhart*, 2008; *Montakhab et al.*, 2012], and the fate of nutrients, organic matter and pollutants in channels[*Schulz et al.*, 2003; *Brookshire and Dwire*, 2003; *Schulz and Peall*, 2001]. To date, sediment transport in bare channels has been extensively investigated, and multiple empirical equations have been proposed to quantify the sediment transport rate in bare channels [e.g., *Yalin*, 2013; *Graf*, 1984]. Most of these equations relate the sediment transport rate to the shear stress at the bed, τ_b, or the friction velocity $U_* = \sqrt{\tau_b/\rho}$, with fluid densityρ [e.g., *Biron et al.*, 2004; *Wilcock*, 1996].

Recently, increasing attention has turned to sediment transport in vegetated channels [e.g., *Jordanova and James*, 2003; *Kothyari et al.*, 2009; *Zong and Nepf*, 2010; *Montakhab et al.*, 2012]. Understanding the impact of vegetation on sediment transport is important because vegetation is a basic component of most natural water environments. In addition, vegetation has been widely used in river restoration both to create habitat and to reduce bank erosion [*Shields et al.*, 1995; *Inoue and Nakano*, 1998; *Abbe et al.*, 2003]. *Sand-Jensen* [1998] observed that streams with vegetation retained up to 80% of the sediment in transit downstream. Similarly, *Warren et al.* [2009] have shown that a vegetated reach retained 50% more corn pollen than an unvegetated reach of similar length. Despite the important role vegetation plays in sediment transport, the impact of vegetation on the flow field and sediment transport is not yet fully understood.

Recent studies suggest that the sediment transport rate in vegetated channels may be related to the bed shear stress τ_b, similar to bare channel flows [*Jordanova and James*, 2003; *Kothyari et al.*, 2009]. However, the typical methods used to estimate the bed shear stress, or the bed friction velocity ($U_* = \sqrt{\tau_b/\rho}$), in a bare channel (listed below) are difficult or not appropriate in vegetated channels, in part because the stress acting on the bed (τ_b) is only a fraction of the total flow resistance. [*Biron et al.*, 2004; *Rowiński and Kubrak*, 2002].

First, methods based on fitting the log law of the wall do not work because the mean velocity profile near the bed is not logarithmic for either submerged or emergent vegetation [*Kundu and Cohen*, 2008; *Nezu and Nakagawa*, 1993; *Nepf*, 2012a; *Liu et al.*, 2008].

Second, the slope method used in bare channels is based on the balance of bed shear stress and the potential forcing due to the water surface slope, i.e. $\tau_b = \rho g s H$, in which g is the gravitational acceleration, H is the water depth, and the potential gradient s is equal to the water surface slope, which for uniform flow is also the bed slope. In vegetated channels, the potential forcing $\rho g s H$ balances both the bed shear stress and the vegetative drag. Some researchers have estimated the bed shear stress by subtracting the vegetative drag from the potential forcing [*Jordanova and James*, 2003; *Kothyari et al.*, 2009]. This method is prone to large uncertainty, because both vegetative drag and the potential forcing are an order of magnitude larger than bed shear stress [*Jordanova and James*, 2003; *Tanino and Nepf*, 2008].

Third, in bare channel flow, the bed shear stress can be estimated from the maximum near-bed Reynolds stress, or by extrapolating the linear profile of Reynolds stress to the bed [*Nezu and Rodi*, 1986]. However, within regions of vegetation the Reynolds stress profile does not increase linearly towards the bed, but rather has a vertical distribution that reflects the distribution of vegetation [*Nepf and Vivoni*, 2000]. It is therefore inappropriate to apply the Reynolds stress method in vegetated channels.

Fourth, in a bare channel the near-bed turbulent kinetic energy (TKE) can be used to estimate the bed shear stress, because the TKE is predominantly generated by shear production at the bed, such that a link exists between the bed shear stress and TKE: $\tau_b \approx 0.2TKE$ [*Stapleton and Huntley*, 1995]. In vegetated channels, however, the turbulence generated by the vegetation dominates the total TKE [*Nepf and Vivoni*, 2000], so that there is no correlation between bed shear stress and turbulent kinetic energy [*Nepf*, 2012b].

Finally, in the case of smooth beds, the bed shear stress may be estimated directly using the velocity gradient at the bed. However, this involves the accurate measurement of the mean velocity profile within the viscous sub-layer, which is technically very difficult.

From the above list, we see that the estimation of bed shear stress in a vegetated channel remains a key limitation in the description of vegetated channel hydraulics. *Rowiński and Kubrak* [2002] proposed a mixing length model to predict the bed shear stress in a channel with emergent vegetation. However, their model requires iteration and does not have a practical form. In this paper, we propose a new model to estimate the bed shear stress in vegetated channels that has the same form in bare channels. It is important to note that our study only considers emergent vegetation, i.e. vegetation that fills the entire water column, and channels with smooth and impermeable beds. Therefore, this is only a first step toward providing a parameterization that will work for field conditions. A discussion on how this model may be extended in the future to channels with non-smooth beds can be found in section 5.

2. Theory

2.1. Governing equations

To account for the spatial heterogeneity of the flow inside a canopy, time- and space-averaged (double-averaged) Navier Stokes (N-S) equations [*Nikora et al.*, 2007, 2013] are commonly employed in the study of both terrestrial canopies [*Finnigan*, 2000; *Raupach and Shaw*, 1982] and aquatic vegetated canopies [*López and García*, 2001; *Luhar et al.*, 2008]. We refer the interested readers to *Nikora et al.* [2007, 2013] for details about the double-averaging method. The double-averaged N-S equations in an emergent canopy of uniform porosity are:

$$\frac{\partial \langle \overline{u_i} \rangle}{\partial x_i} = 0 \tag{1}$$

$$\frac{\partial \langle \overline{u_i} \rangle}{\partial t} + \langle \overline{u_j} \rangle \frac{\partial \langle \overline{u_i} \rangle}{\partial x_j} = g_i - \frac{1}{\rho}\frac{\partial \langle \overline{p} \rangle}{\partial x_i} + \frac{1}{\rho}\frac{\partial}{\partial x_j}\left(\tau_{ij}^{disp} + \left\langle \tau_{ij}^{Rey} \right\rangle + \left\langle \tau_{ij}^{vis} \right\rangle\right) - D_i \tag{2}$$

Here, $u_i = (u, v, w)$ refers to the velocity along the $x_i = (x, y, z)$ axes, corresponding to the stream-wise (parallel to the bed), span-wise, and perpendicular (to the bed) directions, respectively. The $z = 0$ plane corresponds to the smooth bed. The overbar $^-$ indicates a time average, and a single prime $'$ indicates deviation from the time average. The bracket $\langle\rangle$ indicates the spatial average. Each time-averaged variable β is expressed as the sum of the spatial average, $\langle\beta\rangle$, and a deviation from the spatial average β''. p is the pressure, and D_i is the mean vegetative drag in the i direction. τ_{ij}^{disp},τ_{ij}^{Rey},τ_{ij}^{vis} are the dispersive stress, local Reynolds stress and local viscous stress, respectively, defined in Eq.3.

$$\tau_{ij}^{disp} = -\rho \left\langle \overline{u_i}'' \overline{u_j}'' \right\rangle \qquad \tau_{ij}^{Rey} = -\rho \overline{u_i' u_j'} \qquad \tau_{ij}^{vis} = \rho \nu \frac{\partial \overline{u_i}}{\partial x_j} \tag{3}$$

Here ν is the kinematic viscosity. For gradually varying, unidirectional flow in a straight channel, $\left(\langle \overline{u} \rangle \frac{\partial \langle \overline{u} \rangle}{\partial x} \right) / \left(\frac{1}{\rho} \frac{\partial \langle \overline{p} \rangle}{\partial x} \right) \approx \frac{U^2}{gH}$, with U representing the time and cross-sectional averaged velocity. In our experiments, $\frac{U^2}{gH} < 5\%$, so that we neglect the non-uniformity term in the x-momentum equation. Assuming that the average bed-normal($\langle \overline{w} \rangle$) and lateral ($\langle \overline{v} \rangle$) velocity are much smaller than the stream-wise velocity ($\langle \overline{u} \rangle$), and that the flow is steady ($\frac{\partial \langle \overline{u_i} \rangle}{\partial t} = 0$), the stream-wise momentum equation can be simplified to Eq.4.

$$0 = g s_b - \frac{1}{\rho} \frac{\partial \langle \overline{p} \rangle}{\partial x} + \frac{1}{\rho} \frac{\partial}{\partial z} \left(\tau_{ij}^{disp} + \left\langle \tau_{ij}^{Rey} \right\rangle + \left\langle \tau_{ij}^{vis} \right\rangle \right) - D_x \tag{4}$$

Here s_b is the bed slope with respect to a horizontal plane. The vegetative drag D_x can be represented by a quadratic law [e.g., *Nepf*, 2012a]:

$$D_x = \frac{1}{2} \frac{C_D a}{(1 - \phi)} \langle \overline{u} \rangle^2 \tag{5}$$

Here a is the frontal area per canopy unit volume, ϕ is the solid volume fraction, and C_D is the drag coefficient. For cylindrical stems, $\phi = (\pi/4) a d$. Assuming hydrostatic pressure and small bed slope, the pressure gradient can be approximated as $\frac{\partial \langle \overline{p} \rangle}{\partial x} = -\rho g (s_s - s_b)$, where s_s is the water surface slope with respect to a horizontal plane. The fluid shear stresses (τ_{ij}^{disp},τ_{ij}^{Rey},τ_{ij}^{vis}) go to zero at the water surface ($z = Z_s$), so that a vertical integration of Eq. 4 from water surface Z_s to any position $z < Z_s$ yields,

$$\left(\tau_{ij}^{disp} + \left\langle \tau_{ij}^{Rey} \right\rangle + \left\langle \tau_{ij}^{vis} \right\rangle \right) |_z + \rho \int_z^{Z_s} \left[\frac{1}{2} \frac{C_D a}{1 - \phi} \langle \overline{u} \rangle^2 \right] dz = \rho g s \left(Z_s - z \right) \tag{6}$$

Here the potential gradient s is equal to the surface slope s_s. The left-hand side of Eq. 6 shows the partitioning of total flow resistance into the fluid shear stresses (first term) and the vegetation drag (second term). The right-hand side of Eq.6 represents the driving force for the flow due to potential gradient. A similar drag partition is described in [*Raupach and Shaw*, 1982]. The no-slip condition at a smooth impermeable bed requires $\tau_{xz}^{Rey}|_{z=0} = \tau_{xz}^{disp}|_{z=0} = 0$, so that the spatially-averaged bed shear stress is simply $\langle\tau_b\rangle = \left(\tau_{ij}^{disp} + \left\langle\tau_{ij}^{Rey}\right\rangle + \left\langle\tau_{ij}^{vis}\right\rangle\right)|_{z=0} = \left\langle\tau_{xz}^{vis}\right\rangle|_{z=0} = \left\langle\rho\nu\frac{\partial\overline{u}}{\partial z}|_{z=0}\right\rangle$. The effective friction velocity in a heterogeneous flow field can be defined as: $U_{*eff} = \sqrt{\langle\tau_b\rangle/\rho} = \sqrt{\langle\rho {U_*}^2\rangle/\rho} = \sqrt{\langle {U_*}^2\rangle}$, with τ_b and U_* defined as the local bed shear stress and local friction velocity, respectively. In a homogeneous flow field, i.e. without vegetation, $\tau_b = \langle\tau_b\rangle$ and $U_* = U_{*eff} = \langle U_*\rangle$.

2.2. Friction velocity over smooth beds

First, we consider flow over a smooth bed without vegetation, i.e. a bare channel, for which the second term in Eq.6 is absent. In addition, for a bare channel the spatial heterogeneity is small, and therefore the dispersive stress is negligible. Finally, for small s_s and s_b, Z_s is approximately equal to the water depth, H, such that Eq. 6 can be simplified to $\left(\tau_{xz}^{Rey} + \tau_{xz}^{vis}\right)|_z = \rho g s(H - z)$, which indicates that the total stress, the sum of the Reynolds stress and viscous stress, decreases linearly with distance from the bed (z). The same equation is given for bare channels by *Nezu and Nakagawa* [1993]. Note that the local quantities and spatially-averaged quantities are the same in a bare channel. As the Reynolds stress is zero at the bed, $\tau_b = \rho U_*^2 = \tau_{xz}^{vis}|_{z=0} = \rho g s H$, so that the bed shear stress can be estimated from the potential gradient $s = s_s$, which for uniform flow is also the bed slope (s_b). Alternatively, U_* can be estimated by fitting the measured total stress to the theoretical linear distribution of total stress,

$$\tau_{tot}(z) = \left(\tau_{xz}^{Rey} + \tau_{xz}^{vis}\right)|_z = \rho U_*^2(1 - z/H) \tag{7}$$

In this paper, the application of Eq.7 will be called the total stress method.

Another common way to estimate the bed shear stress over a smooth bare channel is to fit the measured velocity to the analytical velocity profile called the Law of the Wall [*Kundu and Cohen*, 2008; *Nezu and Nakagawa*, 1993]:

$$\frac{\overline{u}(z)}{U_*} = \begin{cases} \frac{zU_*}{\nu} = Z_+ & Z_+ \leq 5 \\ \frac{1}{\kappa} ln\left(\frac{zU_*}{\nu}\right) + 5 & Z_+ \geq 30 \end{cases} \tag{8}$$

Here κ, the von Karman constant, is 0.41. This law is linear in the near-bed region ($Z_+ \leq 5$) and logarithmic above ($Z_+ \geq 30$). A buffer layer exists between these two regions, i.e. $5 \leq Z_+ \leq 30$, which is not described by the Law of the Wall.

Within a thin inner layer ($Z_+ \leq 5$), the Law of the Wall assumes that the viscous stress is constant, which is associated with a linear velocity profile (first line of Eq.8). In contrast to this, if we assume that the Reynolds stress is negligible close to the bed, Eq.7 reduces to $(\tau_{xz}^{vis})|_z = \rho gs(H - z)$, indicating that the viscous stress varies linearly with z close to the bed, resulting in a near-bed velocity profile that is parabolic. We define the height of the region dominated by viscous stress, H_v, as the height above the bed at which the linear distribution of viscous stress reaches zero, which corresponds to the height above the bed at which the parabolic portion of the velocity profile ends. Very close to the wall ($Z \ll H_v$), the linear velocity distribution proposed in the Law of the Wall is a good approximation to the parabolic velocity distribution.

The linear viscous stress distribution and the associated parabolic velocity profile can be expressed as:

$$\tau^{vis} = \rho\nu\frac{\partial\overline{u}}{\partial z} = \rho\frac{{U_*}^2}{H_v}(H_v - z) \qquad z \leq H_v \tag{9}$$

$$\overline{u}(z) = \frac{{U_*}^2}{\nu}\left(z - \frac{z^2}{2H_v}\right) \qquad z \leq H_v \tag{10}$$

Note that because the flow is homogeneous in a bare channel, the locally-defined equations (Eq.7, 8, 9 and 10) are also valid for spatially-averaged values, i.e. also apply if the local velocity $\overline{u}$ and the local friction velocity U_* are replaced by the spatially -averaged velocity $\langle \overline{u} \rangle$ and the spatially-averaged friction velocity$\langle U_* \rangle$.

Now we consider the situation with vegetation on a smooth bed. However, we specifically consider regions of the flow for which the distance to the bed is smaller than the distance to the nearest stem, such that the viscous stress and the velocity are controlled by the proximity to the bed in a manner similar to that described above for the bare channel. Namely, the near-bed viscous stress should also follow the linear-stress model. We anticipate that this description will fail at some distance close to a cylinder, at which the cylinder surface also contributes to local viscous stress. In addition, we specifically note that this description will not hold within one diameter of each cylinder (stem), because of secondary flow structures that exist in this region (e.g. [*Stoesser et al.*, 2010]). In a model canopy of emergent vegetation with uniform frontal area (array of circular cylinders), previous studies [*Nepf*, 1999; *Nikora et al.*, 2004; *Liu et al.*, 2008] have shown that the stream-wise velocity in the upper water column (i.e. away from the bed) is vertically uniform, such that $\tau^{vis} = \rho\nu\frac{\partial \overline{u}}{\partial z} = 0$. We therefore propose the following model for the distribution of viscous stress in regions at least one diameter away from the stems inside an emergent canopy:

$$\tau^{vis} = \begin{cases} \rho\frac{{U_*}^2}{H_v}(H_v - z) & z < H_v \\ 0 & z \geq H_v \end{cases} \tag{11}$$

The following velocity distribution is consistent with (11) and a no-slip condition at the bed:

$$\overline{u}\left(z\right)=\begin{cases}\frac{{U_*}^2}{\nu}\left(z-\frac{z^2}{2H_v}\right) & z\leq H_v\\ \frac{{U_*}^2H_v}{2\nu} & z\geq H_v\end{cases}\qquad(12)$$

Denoting the local time-averaged stream-wise velocity in the uniform layer ($z \geq H_v$) as U_o, the local friction velocity U_* can be calculated from Eq. 12.

$$U_*=\sqrt{\frac{2\nu U_o}{H_v}}\qquad(13)$$

In this study, we use laboratory measurement to examine the validity of Eq.13 and to look for connections between H_v and the characteristics of the model canopy. In addition, we evaluate the relationship between the local estimate of U_*, denoted in Eq.13, and the effective friction velocity ($U_{*eff} = \sqrt{\langle {U_*}^2\rangle}$) associated with the spatially-averaged bed shear stress.

3. Methods

Laboratory experiments were conducted in a horizontal recirculating glass flume with a 1.2m-wide and 13m-long test section (bed slope $s_b = 0$). By varying the weir height at the end of the flume, the water depth was varied between $H = 0.07m$ and $H = 0.13m$. By varying the pump frequency, the cross-sectional average velocity was varied between 0.002 and 0.18 m/s. A backscatter Laser Doppler velocimetry (LDV) probe (Dantec Dynamics) was mounted on a manually driven positioning system. Simultaneous measurements of stream-wise (u) and vertical (w) velocity were recorded over a 300s period. The positioning system allowed the LDV to move in both the z and y directions with a resolution of 0.1mm. In order to measure velocity very close to the bed, the LDV axis was tilted 1 deg from horizontal and the velocity was later corrected for this tilt. The wavelengths of the two beams of the LDV were 514.5 and 488nm, and the focal length was 399mm. For the majority of positions the sampling frequency was $125Hz$, but close to the bed the sampling frequency dropped as low as $5Hz$. At this frequency, the mean velocity was still reliably measured, but not the Reynolds stress. In these cases the near bed Reynolds stress measurements were excluded from further anlayses, as noted below. The sampling volume was $4mm \times 0.2mm \times 0.2mm$ in the y, x, and z direction, respectively. The flow was seeded with pliolite particles, and because the PVC board on the bottom of the flume was black, the reflection from the bed was negligible.

To simulate emergent vegetation, rigid dowels were placed in a staggered array with spacing ds. The array was held in place by perforated, black, PVC baseboards with smooth surfaces as shown in Fig.1. The dowels covered the full width of the flume. Two cylinder sizes were considered, with diameter $d = 0.0063m$ and $d = 0.0126m$. The frontal area per unit volume ranged from $a = 0.5m^{-1}$ to $17.8m^{-1}$. The drag coefficient for the cylinders in the array, C_D, was estimated from a previous study [*Tanino and Nepf*, 2008]. 20 trials with dowels and 4 with a bare channel were conducted (Table 1). For each trial, the velocity was measured at 15 to 40 positions along 3 to 11 vertical profiles, with at least 4 profiles for a vegetated channel. Our experiments have shown that in a canopy 4 profiles give a good estimation of the laterally-averaged parameters if the profiles are recorded at the extrema of the velocity field (i.e one profile just behind a dowel $y/ds = 0$, one profile behind the closer adjacent dowel in the upstream row $y/ds = 1$, one profile at the maximum velocity between the two previous dowels $y/ds = 0.5$, and one profile between the maximum velocity and the minimum velocity $y/ds = 0.25$). The vertical spacing of measurements was 0.2mm near the bed. For the denser canopies ($a = 12.6m^{-1}$ and

$17.3m^{-1}$), 2 or 3 dowels at the side of the flume were removed to clear the optical path. Because the cylinders were removed from positions laterally adjacent to the measurement point, their removal did not alter the flow development leading up to the measurement point. Details about each trial can be found in Table 1. Due to the constraint of optical access, the individual vertical profiles were positioned along a lateral transect mid-way between rows. The transect is shown in Fig.1b. In this paper, a spatial-average ($\langle\ \rangle$) denotes the lateral-average along this particular transect. The friction velocity estimated from the spatially-averaged velocity is denoted $\langle U \rangle_*$, and the spatial-average of the local estimates of friction velocity U_*, i.e. based on individual velocity profiles, is denoted $\langle U_* \rangle$. The relationship among $\langle U \rangle_*$, $\langle U_* \rangle$ and U_{*eff} is discussed in section 4.1.2 and 5.1.

The measured velocities were used to estimate the friction velocity by fitting the Law of the Wall (Eq.8), and the new linear stress model (Eq.10 and 12). For the Law of the Wall, U_* was used as the fitting parameter, and the best fit was chosen based on the minimum value of the sum-of-squares error (SSE) between the measurements and the model for both $Z_+ \leq 5$ and $Z_+ \geq 30$ region, i.e. the two regions were fitted together in a single procedure. The uncertainty in the fit was evaluated by finding the range of U_* values that return SSE less than the standard deviation amongst the individual measured profiles. For the new linear stress model, both U_* and H_v were used as fitting parameters for Eq.12 with the best combination of values returning the lowest SSE. The uncertainty of U_* and H_v were tuned separately using the same method as the Law of the Wall. Assuming that the spatially-averaged velocity profile follows the two-layer velocity distribution described by Eq.12, we can also fit $\langle \overline{u} \rangle$ to define an associated $\langle U \rangle_*$ and H_{vo}. The measurements described later in the paper will support this assumption. Correspondingly, $\langle U \rangle_*$ and

H_{vo} were estimated by fitting Eq.12 to the spatially-averaged velocity profile following the same procedure. Finally, for the bare channel cases, the friction velocity was also estimated by fitting Eq.7 over $Z_+ \geq 30$, which we call the total stress method. U_* was chosen based on the minimum SSE between $\rho U_*^2(1 - z/H)$ and $\left(\tau_{xz}^{Rey} + \tau_{xz}^{vis}\right)|_z$ with the stresses estimated from measured velocity data (Eq.3). At $Z_+ \leq 30$, $\left(\tau_{xz}^{Rey} + \tau_{xz}^{vis}\right)|_z$, oscillates intensely with the adjacent value differing by up to 20%. We therefore exclude data from $Z_+ \leq 30$ from the fit. The uncertainty of U_* was then determined from the range of U_* that return a SSE less than the spatial variation between individual local total stress ($\left(\tau_{xz}^{Rey} + \tau_{xz}^{vis}\right)|_z$) profiles. For convenience, the spatially-averaged value were used in all the fittings for bare channel cases, because of the homogeneity of the flow.

4. Results

4.1. Linear distribution of near-bed viscous stress

4.1.1. Flow over a smooth bare channel

We first consider the smooth bare channel. The vertical distribution of normalized spatially-averaged stresses and stream-wise velocity are shown in Fig. 2 for case 1.1. The U_* obtained from the total stress method is used in the normalization. Near the bed ($z_+ \leq H_{v+}$), the viscous stress (triangles) had a linear distribution, supporting the linear stress model described above. For $z_+ = zU_*/\nu \leq 5$ the Law of the Wall and the linear stress model did equally well in describing the measured velocity (compare the gray dashed curve and the black dot-dash curve in Fig.2b). However, unlike the Law of the Wall, the linear stress model also represented the measured velocity for $z_+ \geq 5$, up to $z_+ \approx 25$. That is, the new linear stress model provides a description of the velocity profile that extends through the buffer layer ($5 < Z_+ < 30$).

For the bare channel conditions, three methods were used to estimate the bed shear stress: the Law of the Wall (Eq. 8), the total stress method (Eq.7), and the new linear stress model (Eq. 10). The bed shear stress estimated from the Law of the Wall and the linear stress method agreed within uncertainty (Table 2) for cases 1, 2 and 3, and differed by only 14% for case 4. This agreement makes sense, because near the wall ($Z_+ < 5$), the velocity profiles associated with each fit essentially overlap (Fig. 2b). The total-stress method also produced values of U_* in agreement (within uncertainty) with the two velocity laws, providing a consistency check for the estimated U_*. Finally, the non-dimensional linear-stress layer height, $H_{v+} = H_v U_*/\nu$ (using U_* from the new linear stress model), had a consistent value across all four cases (within uncertainty), suggesting that $H_{v+} = 22 \pm 3(SD)$ may be a universal constant, although further verification is required. Like the viscous sublayer thickness defined in the Law of the Wall ($Z_+ = 5$), H_v, defines a region near the bed dominated by viscous stress, so it is not surprising that it may also have a universal value.

4.1.2. Flow over smooth channels with emergent vegetation

Compared with the bare channel cases, the distribution of stresses within the emergent canopy was more complicated because two additional components were added by the canopy: the dispersive stress and the vegetative drag (Fig. 3a). The vegetative drag, estimated by Eq. 5, represented 97% of the potential forcing and dominated the flow resistance over the entire water column. Because the total stress was dominated by vegetation drag, the total stress normalized by the bed shear stress, $\rho \langle U \rangle_*^2$, was much larger than 1 at the bed. The vertical profiles of viscous stress at eleven positions within the array are shown in Fig. 3b. Although the velocity varied spatially inside the canopy

(Fig. 4 and 5a), the viscous stress had almost no variation along the measurement transect. This gives support to the assumption made above that our transect represents a region of the flow for which the viscous stress distribution is dominated by the proximity to the bed, because the distance to the bed is smaller than the distance to the nearest stem. Further, the viscous stress was linear near the bed and zero in the upper layer (Fig.3b), which agreed with the linear stress model given in Eq.11. The dispersive stress and the Reynolds stress, though comparable to the viscous stress near the bed, reduce to zero at the bed, so the bed shear stress equals the viscous stress at the bed, i.e. the normalized viscous stress goes to 1 (Fig. 3c).

The individual vertical profiles of time-averaged, stream-wise velocity normalized by $\langle U \rangle_*$ at 11 lateral positions are shown in Fig. 4. Here $\langle U \rangle_*$ was derived from the fit of the linear-stress model (Eq.12) to the spatially-averaged velocity profile. At each lateral position, the velocity profiles were consistent with the two-zone profile proposed in Eq. 12. Specifically, the velocity was vertically uniform in the upper canopy ($z/d \geq 4$), and the velocity near the bed ($z/d < 0.5$) was parabolic (gray dot-dash curves in Fig. 4b).

The spatially and time averaged velocity (the black curve in Fig. 5) also supported the linear stress model, i.e. the spatially-averaged velocity was vertically uniform in the upper canopy ($z/d \geq 4$) and parabolic in the near-bed region ($z/d \leq (H_{vo})/d$). Here H_{vo} was derived from the fit of the linear-stress model (Equation 11) to the spatially-averaged velocity profile, the same as $\langle U \rangle_*$. Note again how the parabolic velocity profile provided a good fit to the spatially-averaged velocity over a larger distance (up to $Z_+ = H_{vo} \langle U \rangle_* / \nu = 19$) than the Law of the Wall, which is only valid up to $Z_+ = 5$. However, similar to measurements described in *Liu et al.* [2008] a region of velocity deviation was observed close to $Z_+ = H_{vo+}$. The Reynolds stress exhibited a local maximum at the same distance above the bed (circles, Fig. 3c). The feature deteriorates with increasing lateral distance from the upstream cylinder (Fig.4) suggesting it is associated with the horseshoe or junction vortex formed at the bed near each cylinder base (see Fig.7 in [*Stoesser et al.*, 2010]). These coherent structures scale with the cylinder diameter.

We next consider the relationship between $\langle U \rangle_*$ and H_{vo}, fitted from the spatially-averaged velocity, and the locally fitted U_* and H_v (Fig.6). Along the lateral transect (defined in Fig.1), the local friction velocity $U_*(y)$ was fairly uniform, varying by a maximum of 30% from $\langle U \rangle_*$. The minimum $U_*(y)$ occurred directly behind the upstream dowel ($y = 0$), which was reasonable because the velocity was also minimum here. The spatial-average of the local U_*, denoted as $\langle U_* \rangle$, was approximately equal to $\langle U \rangle_*$ (within 10% uncertainty). To conclude, Fig.4, 5 and 6 taken together have shown that along the measurement transect, the new linear stress model (Eq.11) fits both the local velocity profiles and the spatially-averaged profile. In addition, despite the variation in upper-water column velocity (U_o) across the transect (Fig.5), the friction velocity was fairly constant, such that either order of averaging and fitting ($\langle U \rangle_*$ versus $\langle U_* \rangle$) produced similar values. In the following sections we focus on developing an estimator for $\langle U \rangle_*$. More discussions on how $\langle U \rangle_*$ or $\langle U_* \rangle$ can be used to estimate the effective friction velocity at the canopy scale is presented in section 5.1.

4.2. The scale of H_{vo}

4.2.1. The scale of H_{vo} at low Re_H for $a \geq 4.3m^{-1}$

The values of H_{vo} determined from the linear stress model fit to the spatially-averaged velocity are plotted in Fig.7. Subplot (a) and (b) separate the cases by cylinder diameter,

$d = 6.3$ and $12.6mm$, respectively. First, we consider the smaller cylinder size (Fig.7a). When the array had sufficient density ($a = 4.3m^{-1}$ and $17.3m^{-1}$, shown with squares and up triangles), H_{vo} was comparable to the stem radius (shown by horizontal dashed line). If the depth Reynolds number was not too high ($Re_H \leq 6000$), at similar values of Re_H, H_{vo} in the sparse canopy (gray circles) and the bare channel (open circles) were clearly larger than the stem radius. Therefore the presence of a dense canopy ($a \geq 4.3m^{-1}$) reduced the linear-stress layer thickness to a scale comparable to $d/2$ for small depth Reynolds number (e.g. $Re_H < 6000$). For simplicity, $R = d/2$ is used in the following paragraphs. However, in sparse canopies ($a = 0.5m^{-1}$ in Fig.7a, gray circles), H_{vo} was larger than the stem radius R. Specifically, the sparse canopy value of H_{vo} was between the bare channel value and the value in a dense canopy (R). We propose that at low depth Reynolds number (e.g. $Re_H < 6000$), for canopies of sufficient density (here $a \geq 4.3m^{-1}$), the viscous sub-layer is restricted to the scale of the cylinder radius. The relationship between H_{vo} and R observed for dense canopies ($a \geq 4.3m^{-1}$) is likely associated with the coherent structures formed near the base of each stem. These structures create strong vertical velocity near the bed, as shown by *Stoesser et al.* [2010]. In particular, Fig.5 in *Stoesser et al.* [2010] shows strong vertical velocity occurs near $z = R$. By enhancing vertical momentum transport near the bed, the coherent structures may suppress H_{vo} to a scale comparable to R.

4.2.2. Dependence on Re_H

As Re_H increased, the bare channel values of H_{vo} decreased (Fig.7a), which is consistent with the constant value observed for $H_{vo+} = (H_{vo} \langle U \rangle_*)/\nu = 22 \pm 3$ (Table 2). As $\langle U_o \rangle$ increases, $\langle U \rangle_*$ also increases, so that H_{vo} decreases. The same trend was observed for the viscous sub-layer defined by the Law of the Wall (δ_s), i.e. $\delta_{s+} = 5$, so that as $\langle U_o \rangle$ increases, δ_s decreases. In our study, H_{vo} in the bare channel became comparable to the smaller stem radius ($d = 6.3mm$) near $Re_H = 8000$ (Fig.7a), so that above this value of Re_H, the presence of the canopy had little impact on the value of H_{vo}. Although not evident in the cases we tested, we conjecture that if Re_H was increased further ($Re_H > 8000$), the bare channel H_{vo} would become smaller than R. Accordingly, we posit that there exists a Reynolds number above which the linear-stress layer thickness, H_{vo}, would be the same in both bare and vegetated channels, because the constraint imposed on H_{vo} by bed-generated turbulence would be greater than the constraint imposed by the stem-generated turbulence.

Now we consider the larger size cylinders ($d = 12.6mm$, Fig.7b). The values of H_{vo} observed with the larger diameter arrays were consistent with conclusions drawn above based on the smaller diameter arrays. Because the size constraint imposed by the stem radius was larger ($R = 6.3mm$), the bare channel value of H_{vo} became comparable to R at a lower Re_H than occurred with the smaller radius arrays ($R \approx 3.2mm$). Specifically, the bare and vegetated channel values of H_{vo} became comparable to one another within uncertainty at $Re_H = 4000$. At higher Re_H, there was no difference between the bare channel and emergent array conditions. To summarize, below a transition Re_H, a dense canopy ($a \geq 4.3m^{-1}$) can suppress H_{vo} to R, but at higher Re_H, H_{vo} is the same in both bare and vegetated channels. The transition Re_H decreases with increasing stem radius. Based on this, we suggest that the linear-stress layer thickness in a dense canopy ($a \geq 4.3m^{-1}$) will be $H_{vo} = min\,(R, 22\nu/\langle U \rangle_*)$, where the later term denotes the value for a bare bed.

The fitted H_{vo} normalized by $min\left(R, 22\nu/\left\langle U\right\rangle_*\right)$ are shown in Fig.8. For the bare channel and emergent channels with $a \geq 4.3m^{-1}$, the model gives a very robust prediction of H_{vo}, with these cases falling along the line of model agreement, shown by the horizontal dashed line. The proposed model for H_{vo} fails for sparse arrays ($a = 0.5m^{-1}$, gray circles).

4.3. Estimation of $\left\langle U\right\rangle_*$ in an emergent canopy

As shown in Fig.5, the spatially-averaged velocity can also be fit to Eq.13, producing the estimate $\left\langle U\right\rangle_* = \sqrt{\frac{2\nu\langle U_o\rangle}{H_{vo}}}$. Below the transition Re_H, which varies with stem radius and bed texture, we propose that the friction velocity $\left\langle U\right\rangle_* = 2\sqrt{\frac{\nu\langle U_o\rangle}{d}}$. As discussed above, this scaling fails if the canopy is too sparse, such that the stem-scale coherent structures do not dominate the near-bed flow, or if the depth Reynolds number is too high, such that the bed-driven turbulence places a stronger constraint on H_{vo} than the stem related turbulence. To reflect the influence of both bed-driven and stem-driven near-bed turbulence, we propose the following relationship for dense emergent canopies:

$$\left\langle U\right\rangle_* = max\left(\sqrt{C_f}\left\langle U_o\right\rangle, 2\sqrt{\frac{\nu\left\langle U_o\right\rangle}{d}}\right) \tag{14}$$

Here, C_f denotes the drag coefficient for the bare bed, and is a function of bed texture. Note that although $\left\langle U_o\right\rangle$ strictly defines the spatial-average of the velocity in the uniform upper layer of the canopy, in most cases $\left\langle U_o\right\rangle$ is close to the cross-sectionally averaged velocity, which is denoted as U in Table 1, which is also the volume flow rate per unit cross-sectional area corrected for porosity. Eq.14 captures the physical limit that at high Reynolds number the vegetation will have negligible influence on H_{vo} and $\left\langle U\right\rangle_*$. This limit is demonstrated in the values of $\left\langle U\right\rangle_*$ shown in Fig. 9a. For the two stem diameters we studied, when Re_H was higher than 8000, the non-dimensional friction velocity $\left\langle U\right\rangle_* / \left\langle U_o\right\rangle$

in the emergent canopy was close to the value observed in the bare channel, regardless of the stem diameter and the density of the canopy. However, at low and moderate Re_H, $\langle U \rangle_* / \langle U_o \rangle$ in dense canopies (squares, triangles, and pentagrams) was higher than bare channel values in Fig. 9a. Note that the transition Re_H should decrease as d increases. That is, for a larger stem diameter, the bare channel value of H_{vo} would reach R at a lower Re_H. We caution that the transition Re_H will likely also depend on the bare bed texture which influences C_f. The quantification of C_f, however, was not the focus of this study. Here we assume that C_f for the bare channel is already known, and concentrate on quantifying the bed shear stress once cylinder arrays have been added to the bare bed.

Finally, Fig. 9b depicts $\langle U \rangle_*$ non-dimensionalized by $\sqrt{(\nu \langle U_o \rangle)/d}$ for $Re_H \leq 6000$. Over this range of Re_H, $\langle U \rangle_* / \langle U_o \rangle$ was enhanced by dense canopies with stem diameter $d = 6.3mm$ (the squares and up triangles in Fig. 9a). Compared with the scatter of $\langle U \rangle_* / \langle U_o \rangle$ over the same range of Re_H shown in Fig. 9a, the $\langle U \rangle_*$ non-dimensionalized by $\sqrt{(\nu \langle U_o \rangle)/d}$ was roughly a constant (≈ 2) as shown in Fig. 9b. This observation confirmed that for this range of conditions $\langle U \rangle_*$ might be estimated as $\langle U \rangle_* \approx 2\sqrt{(\nu \langle U_o \rangle)/d}$. In order to test the robustness of the conceptual model, the $\langle U \rangle_*$ obtained from Eq.14 normalized by $\langle U_o \rangle$ was plotted again the fitted $\langle U \rangle_*$ normalized by $\langle U_o \rangle$ in Fig.10. As shown in the figure, $\langle U \rangle_* / \langle U_o \rangle$ for the bare bed cases (open circles) collapse to a single point, indicating that $\langle U \rangle_* / \langle U_o \rangle$ is a constant for bare bed channels with the same bed texture. In the channels with model vegetation, however, $\langle U \rangle_* / \langle U_o \rangle$ has a wide range of values. The proposed model (Eq.14 and the dashed line in Fig.10) captures the variation of $\langle U \rangle_* / \langle U_o \rangle$ in an emergent canopy with density $a \geq 4.3m^{-1}$. For $a = 0.5m^{-1}$, however, the model over-predicts $\langle U\rangle_* / \langle U_o\rangle$. More extensive testing is needed to more precisely define the array density above which Eq.14 applies.

5. Discussion

5.1. Relationship between the measurement transect and the canopy average

As discussed in section 4.1.2, the friction velocity $\langle U\rangle_*$, fitted from the spatially-averaged velocity $\langle U\rangle$ along the measurement transect (Fig. 1), falls within 10% of $\langle U_*\rangle$, the spatial-average of the local U_* (Fig.6). In this section, we use the numerically simulated data from *Salvador et al.* [2007] to show that $\langle U_*\rangle$ may be a good approximation for the effective friction velocity U_{*eff} ($= \sqrt{\langle U_*^2\rangle}$) within some uncertainty. The simulation results are shown in Fig.11. We first exclude the data in the region within one diameter from the center of each stem (Fig.11). We justify this exclusion based on the fact that we seek an estimate of bed shear stress for the future purpose of predicting net sediment flux through the canopy. The elevated (red) and diminished (blue) regions of bed stress close to the individual cylinders only produce localized sediment transport, i.e. the scour holes and deposition mounds classically observed near bridge piers (Fig.1 in [*Yager*, 2013]), and are not indicators of sediment flux at the canopy scale. Specifically, *Hongwu et al.* [2013] observed that the generation of individual scour holes occurs at lower channel velocities than the onset of canopy-scale sediment transport. Therefore, we suggest that the value of bed shear stress within the contiguous region of relatively uniform bed shear stress (green region in the color map) represents the more relevant value for predicting canopy-scale sediment transport.

After excluding data from within 1 diameter of each stem center, we laterally-averaged the local U_* at each x position (upper plot in Fig.11). This lateral-average of local U_* is denoted as $\langle U_* \rangle_L$. The position $x/ds = 1$ corresponds to the measurement transect used in this study, and this point is marked in Fig.11. The average of $\langle U_* \rangle_L$ along the x direction, denoted as $\langle U_* \rangle_A$, is the canopy-scale area average of U_*. Fig.11 shows the variation $\langle U_* \rangle_L$, normalized by the shear velocity associated with the total stress $\sqrt{gHs}$, along x (blue curve). Note that since vegetative drag also contributes to the total stress, this normalized bed shear stress has an average value less than 1. In the region between cylinders, e.g. $x/ds = 0.5$ to 1.5, $\langle U_* \rangle_L$ is relatively uniform, and close to $\langle U_* \rangle$ (marked in figure). Further, $\langle U_* \rangle$ differs from $\langle U_* \rangle_A$ (blue dashed line) by only 10%. For arrays with larger spacing between cylinders, the uniform region will occupy a larger fraction of the total area, and the difference between $\langle U_* \rangle$ and $\langle U_* \rangle_A$ will decrease. We therefore tentatively suggest that $\langle U_* \rangle$ is representative of the canopy-average. In addition, the effective friction velocity, defined as $U_{*eff} = \sqrt{\langle U_*^2 \rangle}$ (black dashed line Fig.11) is approximately equal to the $\langle U_* \rangle_A$ (within 5%). Given this, we suggest that Eq.14 may reasonably predict the effective friction velocity U_{*eff}:

$$U_{*eff} = max\left(\sqrt{C_f}\,\langle U_o \rangle\,, 2\sqrt{\frac{\nu\,\langle U_o \rangle}{d}}\right) \tag{15}$$

We caution that this conclusion is tentative, because *Salvador et al.* [2007] only provides maps of bed shear stress for a single case, $Re_H \approx 3000$ and $ds = 2.5d$.

5.2. Limitations of the model

The linear-stress model developed in this study has several limitations. Firstly, it only works when the frontal area per unit canopy volume a is large enough so that the velocity in the upper water column is uniform and that the stem generated turbulence is strong enough to limit the scale of H_v to R. In our experiments, we found that these conditions are met for $a \geq 4.3m^{-1}$.

Secondly, the vegetation center-to-center spacing $2ds$ (as shown in Fig.1) should be larger than twice the stem diameter $2d$. As discussed in section 2.2, within one diameter of the stem center, the local linear stress model does not hold because the horseshoe vortex system generated at the stem base locally alters the stress distribution. In addition, as the center-to-center spacing ($2ds$) decreases below $5d$, the case shown in Fig.11, the region where $\langle U_* \rangle_L$ is uniform also decreases. As a result the difference between $\langle U_* \rangle$ and U_{*eff} would increase, degrading the accuracy of the shear-stress estimate given in Eq.15. However, for $ds/d = 2.5$, the difference between $\langle U_* \rangle$ and U_{*eff} is only 15% (Fig.11), implying that Eq.15 is accurate to within 15%.

Thirdly, the model and experiments described here only consider smooth and impermeable beds. Using the distinction between hydraulically rough and smooth flows as a guide, we expect that the validity of the proposed model for rough beds would depend on the relative size of the bed roughness (sediment size) and thickness of the linear-stress layer. For example, in a salt marsh, $\langle U_o \rangle$ may be between 1 and $10cm/s$ and typical stem sizes are $d = 0.1$ to $1cm$, such that the thickness of the linear-stress layer $H_{vo} = min\left(R, 22\nu/\sqrt{C_f}\,\langle U_o \rangle\right)$ is on the order of 1mm, which is larger than the sediment size (on the order of 0.1mm). In this case the model developed for smooth beds may provide a reasonable estimate of U_*. In contrast, on a floodplain $\langle U_o \rangle$ may be $1m/s$ or higher and d is O($10cm$), so that H_{vo} is on the order of 0.1mm which is comparable to sediment size. In this case, the bed roughness extends beyond what we expect to be the linear-stress layer, and we expect that the bed roughness will alter near-bed dynamics. Possibly this adjustment may be accomplished with an adjustment to C_f to reflect the appropriate roughness, but a firm conclusion cannot be drawn until experiments are completed on rough, permeable beds.

It is important to note that the spatial-averaging discussed in this paper (and especially section 5.1) was targeted only at bed shear stress. The relationships between local values and area-averages cannot be extended to other quantities, such as velocity or dispersive stress. In addition, the model here only considers emergent vegetation with cylindrical geometry. To apply the model for submerged vegetation, the frontal area index ah (h is the height of the vegetation) has to satisfy $ah \geq 0.3$ so that the turbulence generated at the top of the submerged canopy does not penetrate to the bed and affect the near bed stress distribution ([*Luhar et al.*, 2008]). For vegetation with non-uniform frontal area, $a(z)$, the velocity in the upper layer of the canopy will not be uniform, instead varying inversely with a in z direction [*Nikora et al.*, 2004]. In this case, the upper layer velocity $\langle U_o \rangle$ will need to be defined more carefully.

6. Conclusion

This study developed a model that can predict the friction velocity in smooth channels with and without model emergent vegetation. In a bare channel, the model assumes that within a distance H_v from the bed, the Reynolds stress is negligible so that the viscous stress decreases linearly with increasing distance from the bed. The experimental data confirm the near-bed linear distribution of viscous stress and suggest a universal value for the non-dimensional layer thickness $H_{v+} = 22 \pm 3$. Within a model canopy of emergent cylindrical dowels, the linear stress distribution was observed in regions more than one diameter from the center of each dowel (Fig.4). For canopy density above $4.3 m^{-1}$, the thickness of the linear stress layer (H_v) was shown to be the minimum of the stem radius ($d/2$) and the bare channel value ($22\nu/\langle U\rangle_*$), such that the effective friction velocity can be estimate from $U_{*eff} = max\left(\sqrt{C_f}\langle U_o\rangle, 2\sqrt{\frac{\nu\langle U_o\rangle}{d}}\right)$. The effective friction velocity in an emergent canopy is therefore either larger than or equal to the bare channel value, for comparable depth-average velocity.

Acknowledgments. The work was supported by NSF Grant EAR 1414499. The data for the color map in Fig.11 is provided by Guillermo Palau Salvador, Thorsten Stoesser, Andreas Christof Rummel, and Wolfgang Rodi. The velocity data used in the paper is available in excel format upon request from the authors. The data are archived at MIT Parsons Lab. We also thank Francesco Ballio and two other anonymous reviewers for their useful comments.

References

Abbe, T. B., A. P. Brooks, and D. R. Montgomery (2003), Wood in river rehabilitation and management. *The Ecology and Management of Wood in World Rivers* (eds S. V. Gregory, K.L. Boyer & A.M. Gurnell), pp. 367-389. Paper presented at Symposium 37. American Fisheries Society, Bethesda, MD.

Bennett, S. J., W. Wu, C. V. Alonso, and S. S. Wang (2008), Modeling fluvial response to in-stream woody vegetation: implications for stream corridor restoration, *Earth Surface Processes and Landforms*, *33*(6), 890–909.

Biron, P. M., C. Robson, M. F. Lapointe, and S. J. Gaskin (2004), Comparing different methods of bed shear stress estimates in simple and complex flow fields, *Earth Surface Processes and Landforms*, *29*(11), 1403–1415.

Brookshire, E. J., and K. A. Dwire (2003), Controls on patterns of coarse organic particle retention in headwater streams, *Journal of the North American Benthological Society*, *22*(1), 17–34.

Christiansen, C., H. Christoffersen, J. Dalsgaard, and P. NØrnberg (1981), Coastal and near-shore changes correlated with die-back in eel-grass (*Zostera Marina, L.*), *Sedimentary Geology*, *28*(3), 163–173.

Finnigan, J. (2000), Turbulence in plant canopies, *Annual Review of Fluid Mechanics*, *32*(1), 519–571.

Gacia, E., and C. M. Duarte (2001), Sediment retention by a mediterranean *Posidonia oceanica Meadow*: The balance between deposition and resuspension, *Estuarine, Coastal and Shelf Science*, *52*(4), 505–514.

García, M. (2008), *Sedimentation engineering: processes, measurements, modeling, and practice. 2008*, ASCE Publications.

Graf, W. H. (1984), *Hydraulics of sediment transport*, Water Resources Publication.

Hongwu, Tang and Wang, H and Liang, DF and Lv, SQ and Yan, L (2013), Incipient motion of sediment in the presence of emergent rigid vegetation, *Journal of Hydro-environment Research*, *7*(3), 202–208.

Inoue, M., and S. Nakano (1998), Effects of woody debris on the habitat of juvenile masu salmon (oncorhynchus masou) in northern japanese streams, *Freshwater Biology*, *40*(1), 1–16.

Jordanova, A. A., and C. James (2003), Experimental study of bed load transport through emergent vegetation, *Journal of Hydraulic Engineering*, *129*(6), 474–478.

Kothyari, U. C., H. Hashimoto, and K. Hayashi (2009), Effect of tall vegetation on sediment transport by channel flows, *Journal of Hydraulic Research*, *47*(6), 700–710.

Kundu, P., and I. Cohen (2008), *Fluid Mechanics. 2004*, Elsevier Academic Press.

Lenhart, C. F. (2008), *The Influence of Watershed Hydrology and Stream Geomorphology on Turbidity, Sediment and Nutrients in Tributaries of the Blue Earth River, Minnesota, USA.*, ProQuest.

Liu, D., P. Diplas, J. Fairbanks, and C. Hodges (2008), An experimental study of flow through rigid vegetation, *Journal of Geophysical Research: Earth Surface (2003–2012)*, *113*(F4).

López, F., and M. H. García (2001), Mean flow and turbulence structure of open-channel flow through non-emergent vegetation, *Journal of Hydraulic Engineering*, *127*(5), 392–402.

Luhar, M., J. Rominger, and H. Nepf (2008), Interaction between flow, transport and vegetation spatial structure, *Environmental Fluid Mechanics*, *8*(5-6), 423–439.

Montakhab, A., B. Yusuf, A. Ghazali, and T. Mohamed (2012), Flow and sediment transport in vegetated waterways: a review, *Reviews in Environmental Science and Bio/Technology*, *11*(3), 275–287.

Nepf, H. (1999), Drag, turbulence, and diffusion in flow through emergent vegetation, *Water resources research*, *35*(2), 479–489.

Nepf, H., and E. Vivoni (2000), Flow structure in depth-limited, vegetated flow, *Journal of Geophysical Research: Oceans (1978–2012)*, *105*(C12), 28,547–28,557.

Nepf, H. M. (2012a), Flow and transport in regions with aquatic vegetation, *Annual review of fluid mechanics*, *44*, 123–142.

Nepf, H. M. (2012b), Hydrodynamics of vegetated channels, *Journal of Hydraulic Research*, *50*(3), 262–279.

Nezu, I., and H. Nakagawa (1993), *Turbulence in open-channel flows*, Rotterdam: Balkema.

Nezu, I., and W. Rodi (1986), Open-channel flow measurements with a laser doppler anemometer, *Journal of Hydraulic Engineering*, *112*(5), 335–355.

Nikora, V., F. Ballio, S. Coleman, and D. Pokrajac (2013), Spatially averaged flows over mobile rough beds: definitions, averaging theorems, and conservation equations, *Journal of Hydraulic Engineering*, *139*(8), 803–811.

Nikora, V., I. McEwan, S. McLean, S. Coleman, D. Pokrajac, and R. Walters (2007), Double-averaging concept for rough-bed open-channel and overland flows: Theoretical background, *Journal of Hydraulic Engineering*, *133*(8), 873–883.

Nikora, V., K. Koll, I. McEwan, S. McLean, and A. Dittrich (2004), Velocity distribution in the roughness layer of rough-bed flows, *Journal of Hydraulic Engineering*, *130*(10), 1036–1042.

Raupach, M., and R. Shaw (1982), Averaging procedures for flow within vegetation canopies, *Boundary-Layer Meteorology*, *22*(1), 79–90.

Robbins, C. H., and A. Simon (1983), Man-induced channel adjustment in tennessee streams, *Tech. rep.*, United States Geological Survey.

Rowiński, P. M., and J. Kubrak (2002), A mixing-length model for predicting vertical velocity distribution in flows through emergent vegetation, *Hydrological sciences journal*, *47*(6), 893–904.

Salvador, P. G., T. Stoesser, A. Rummel, and W. Rodi (2007), Turbulent shallow flow through vegetation, *IProc. IAHR Fifth International Symposium on Environmental Hydraulics (ISEH V), Arizona, USA.*

Sand-Jensen, K. (1998), Influence of submerged macrophytes on sediment composition and near-bed flow in lowland streams, *Freshwater Biology*, *39*(4), 663–679.

Schulz, M., H.-P. Kozerski, T. Pluntke, and K. Rinke (2003), The influence of macrophytes on sedimentation and nutrient retention in the lower river spree (germany), *Water Research*, *37*(3), 569–578.

Schulz, R., and S. K. Peall (2001), Effectiveness of a constructed wetland for retention of nonpoint-source pesticide pollution in the lourens river catchment, south africa, *Environmental science & technology*, *35*(2), 422–426.

Shields, F., A. Bowie, and C. Cooper (1995), Control of streambank erosion due to bed degradation with vegetation and structure1, *JAWRA Journal of the American Water Resources Association*, *31*(3), 475–489.

Shields Jr, F. D., N. Morin, and C. M. Cooper (2004), Large woody debris structures for sand-bed channels, *Journal of Hydraulic Engineering*, *130*(3), 208–217.

Stapleton, K., and D. Huntley (1995), Seabed stress determinations using the inertial dissipation method and the turbulent kinetic energy method, *Earth Surface Processes and Landforms*, *20*(9), 807–815.

Stoesser, T., S. Kim, and P. Diplas (2010), Turbulent flow through idealized emergent vegetation, *Journal of Hydraulic Engineering*, *136*(12), 1003–1017.

Tanino, Y., and H. M. Nepf (2008), Laboratory investigation of mean drag in a random array of rigid, emergent cylinders, *Journal of Hydraulic Engineering*, *134*(1), 34–41.

Warren, L. L., R. S. Wotton, G. Wharton, J. A. Bass, and J. A. Cotton (2009), The transport of fine particulate organic matter in vegetated chalk streams, *Ecohydrology*, *2*(4), 480–491.

Wilcock, P. R. (1996), Estimating local bed shear stress from velocity observations, *Water Resources Research*, *32*(11), 3361–3366.

Yager, E., and M. Schmeeckle (2013), The influence of vegetation on turbulence and bed load transport, *Journal of Geophysical Research: Earth Surface*, *118*(3), 1585–1601.

Yalin, M. S. (2013), *Mechanics of sediment transport*, Pergamon press.

Zong, L., and H. Nepf (2010), Flow and deposition in and around a finite patch of vegetation, *Geomorphology*, *116*(3), 363–372.

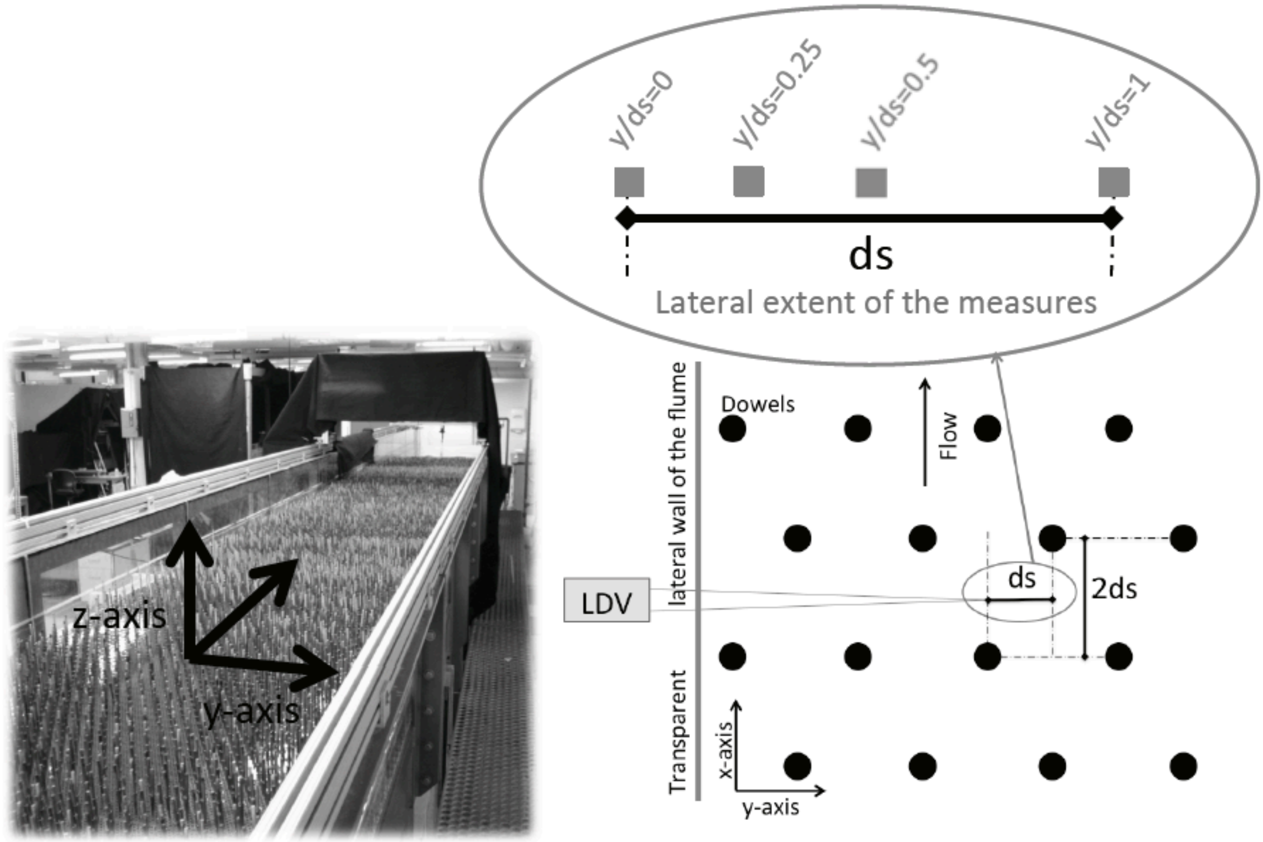

Figure 1. Experimental set-up. The LDV measured streamwise (u) and vertical (w) velocity. Vertical profiles were recorded at different lateral positions along the transect of length ds (shown above) positioned at the mid-point between two rows of wood dowels.

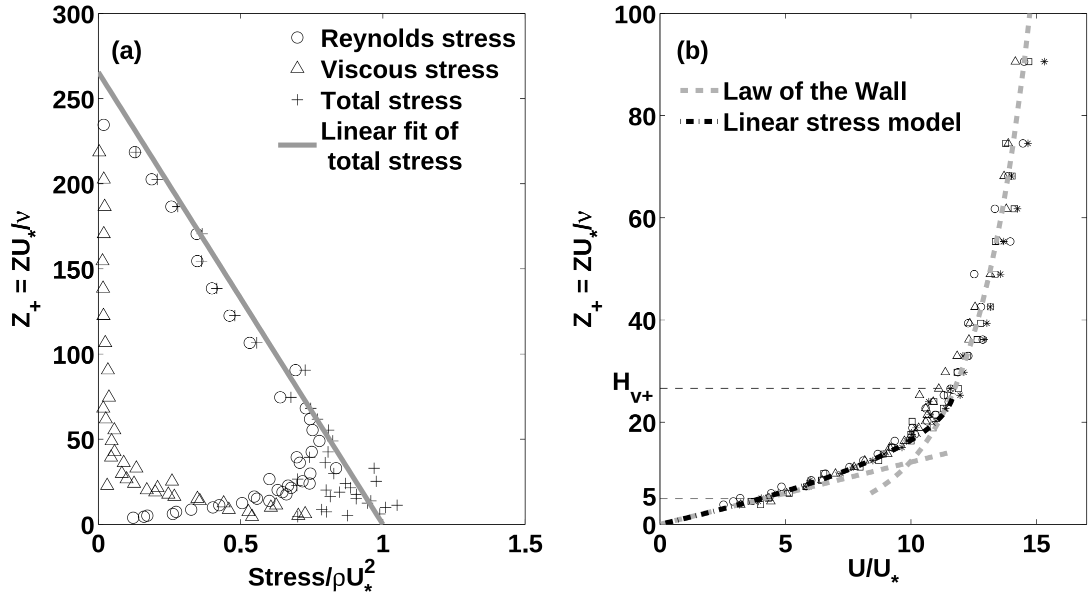

Figure 2. (a) Spatially-averaged stresses normalized by ρU_*^2 with U_* estimated from the total stress method, and (b) stream-wise velocity normalized by U_* at four horizontal locations (symbols) for case 1.1. The four locations are 5cm apart along a lateral transect in the middle of the flume. The near-bed viscous stress (triangles) follows a linear distribution. The linear fit to the total stress (gray solid line) represents the total stress method for U_* in Table 1. The time averaged stream-wise velocity profiles at four lateral positions are presented by four different symbols in figure (b). The velocity follows the Law of Wall (gray dashed curves in b) in the near bed region and the upper log-layer region. The new linear stress model (black dot-dash parabola) follows the measured velocity up to $z = H_{v+} \approx 25$.

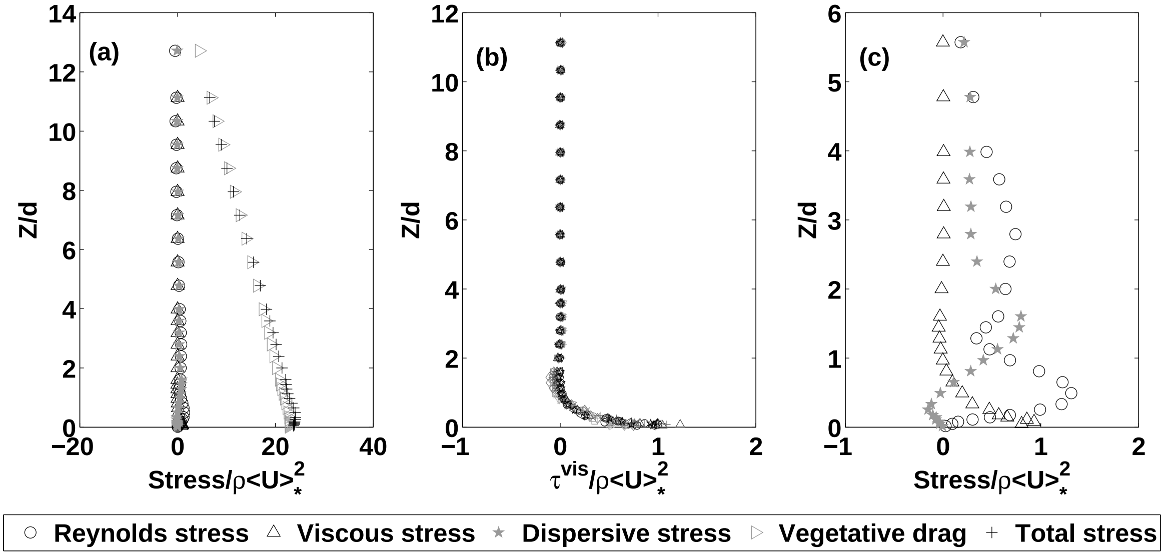

Figure 3. Emergent canopy case 3.1, $a = 4.3m^{-1}$, $ds = 3d$, $U = 0.052m/s$. The stem diameter for this case is 0.0063m, and the fitted linear-stress layer thickness $H_{vo} = 0.0035m$, corresponding to $H_{vo}/d = 0.56$. The vertical axis is the distance from the bed normalized by the stem diameter, and the horizontal axes are the stresses normalized by $\rho \langle U \rangle_*^2$, the bed shear stress fitted from the spatially-averaged velocity profile. (a) The spatially averaged stress distribution is shown with the vegetative drag calculated with Eq. 5 using drag coefficients C_D estimated from a previous study by *Tanino and Nepf* [2008]. Because the total stress is dominated by vegetation drag, the total stress normalized by the bed shear stress, $\rho \langle U \rangle_*^2$, is much larger than 1 at the bed. (b) Viscous stress profiles measured at 11 horizontal positions (symbols). (c) Spatially averaged stresses.

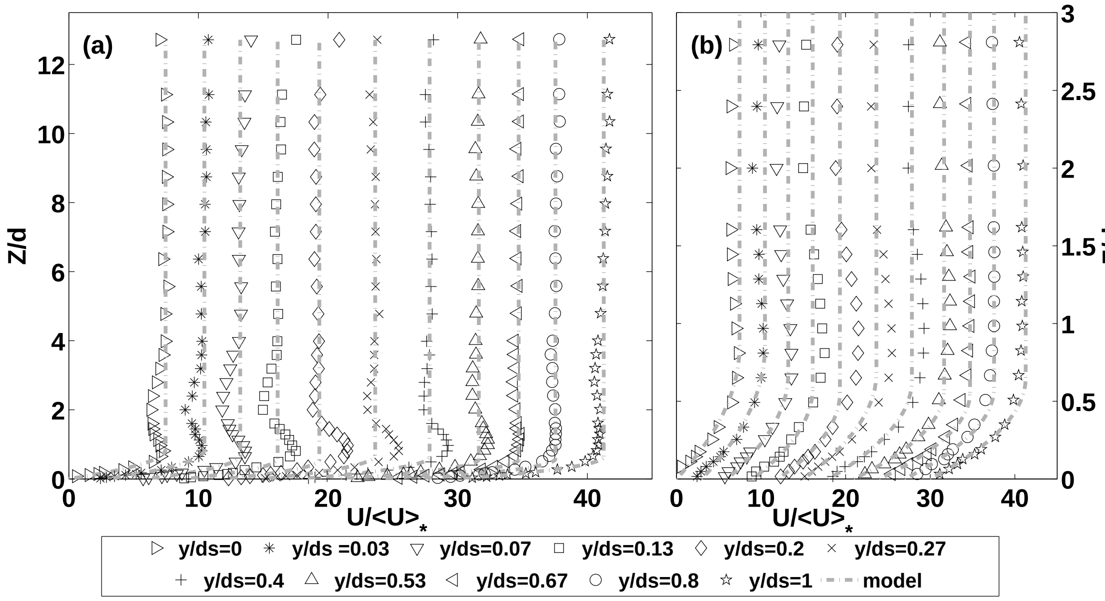

Figure 4. Case 3.1 (as in Fig.3). Vertical profiles of time-averaged stream-wise velocity normalized by $\langle U \rangle_*$ at 11 horizontal positions (symbols). The x-axis of each profile is offset by 3 units. The gray dot-dash curves represent the fit of the linear-stress model (Equation 11) to each individual profile. (a) The velocity distribution over the whole water depth. In the upper layer, the velocity is vertically uniform. (b) The velocity distribution in the near bed region. The velocity is parabolic very close to the wall.

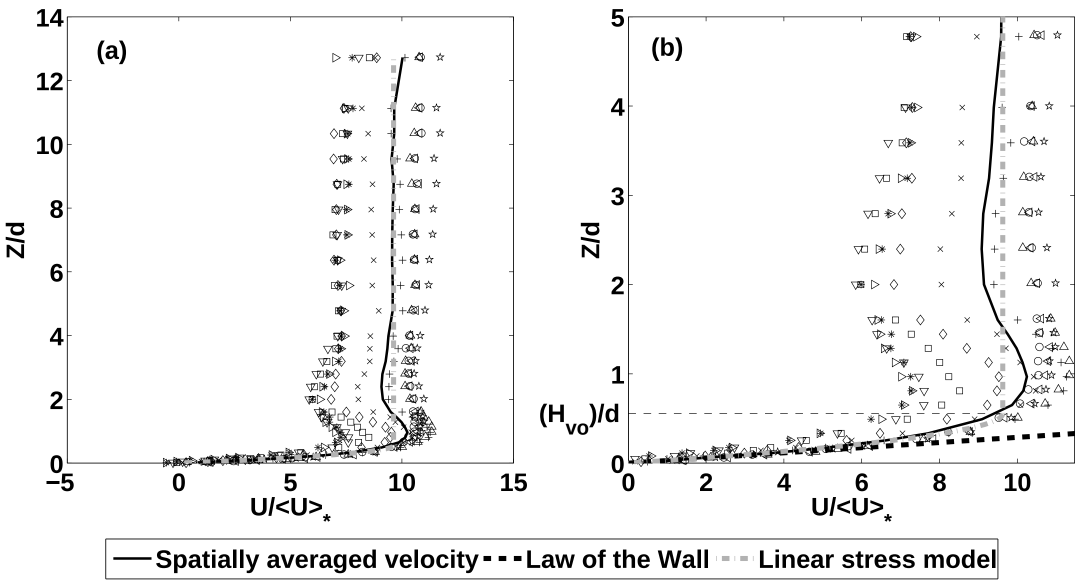

Figure 5. Case 3.1. Vertical profiles of time-averaged stream-wise velocity normalized by $\langle U \rangle_*$ at 11 horizontal positions (symbols shown in Fig.4) and the spatial-average (shown with heavy black curve). The gray dot-dash curve represents the fit of the linear-stress model (Equation 11) to the spatially-averaged velocity profile. The black dashed line represents the fit of the linear part of the Law of the Wall (Equation 7) to the spatially-averaged velocity. (a) In the upper layer, the spatially-averaged velocity is constant except in regions very close to the surface. (b) The distribution of the spatially-averaged velocity in the near bed region is parabolic up to $H_{vo}/d \approx 0.5$.

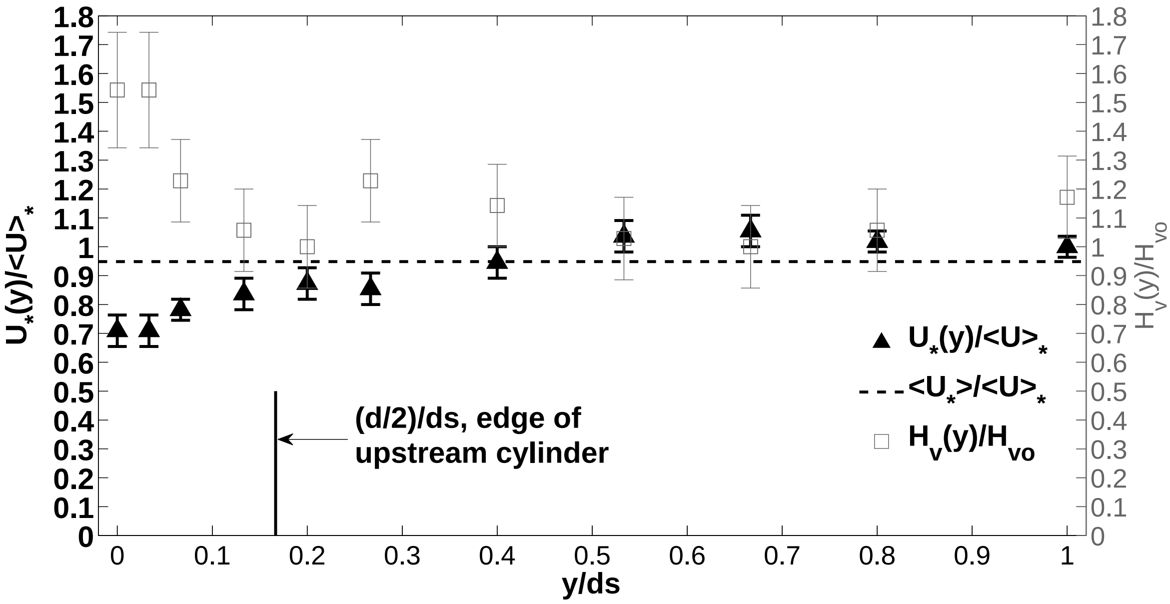

Figure 6. Case 3.1. The distribution of the $U_*(y)$, fitted from local velocity profile, normalized by $\langle U \rangle_*$ (triangles), and the distribution of the locally fitted $H_v(y)$ normalized by H_{vo} (squares). Here y indicates the position in the lateral transect, with $y = 0$ right behind the dowels as shown in Fig. 1. The horizontal dashed line represents the spatial-average of local $U_*(y)$ normalized by $\langle U \rangle_*$.

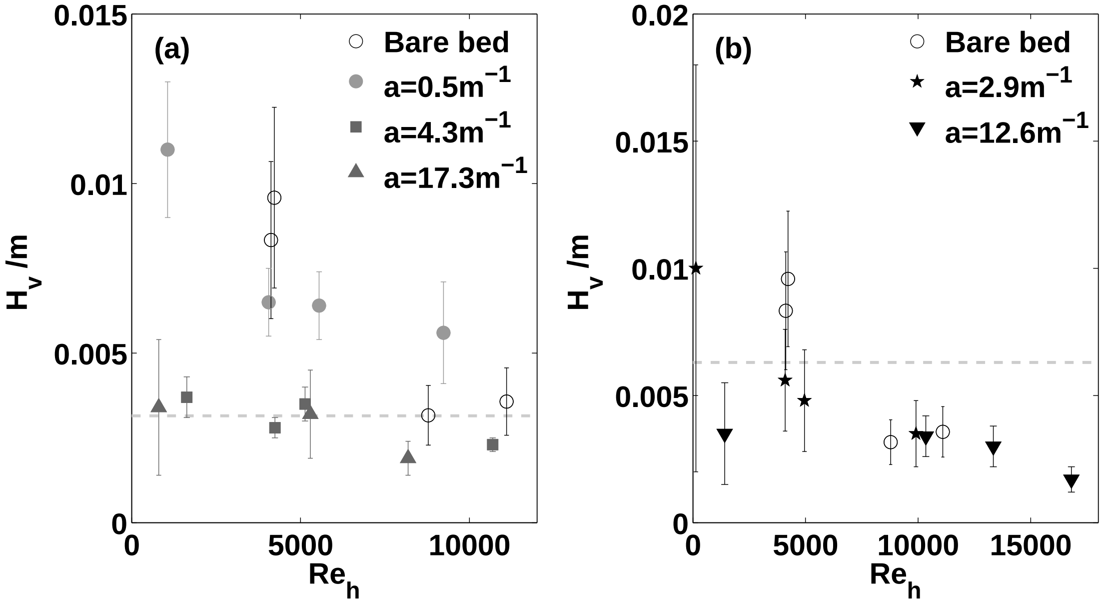

Figure 7. The linear-stress layer thickness, H_{vo}, versus depth Reynolds number, Re_H, for the bare channel cases (open circles) and the vegetation cases (a) with stem diameter d=6.3 mm and (b) with stem diameter d=12.6mm. The depth Reynolds number Re_H is calculated using the spatially-averaged upper-layer velocity $\langle U_o \rangle$ for the vegetated cases and the cross-sectionally-averaged velocity for the bare channel cases. The vertical error bars represent the uncertainty in fitting H_{vo}.

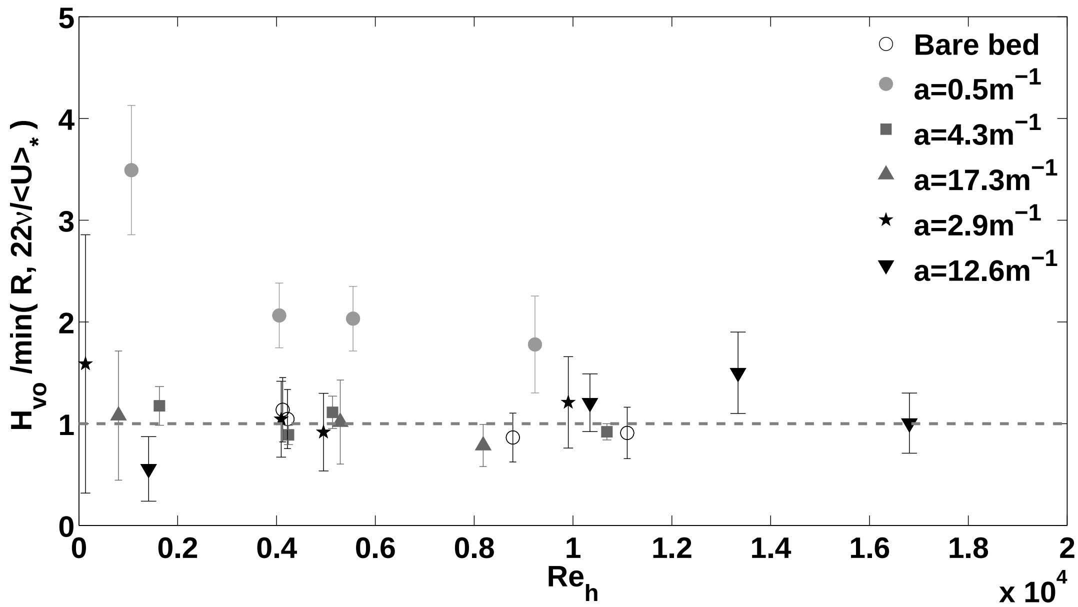

Figure 8. The fitted H_{vo} normalized by the proposed model $min\left(R, 22\nu/\left\langle U\right\rangle_*\right)$. The dashed line indicates agreement with the proposed model. The vertical errorbars represent the fitting errors of H_{vo} normalized by $min\left(R, 22\nu/\left\langle U\right\rangle_*\right)$.

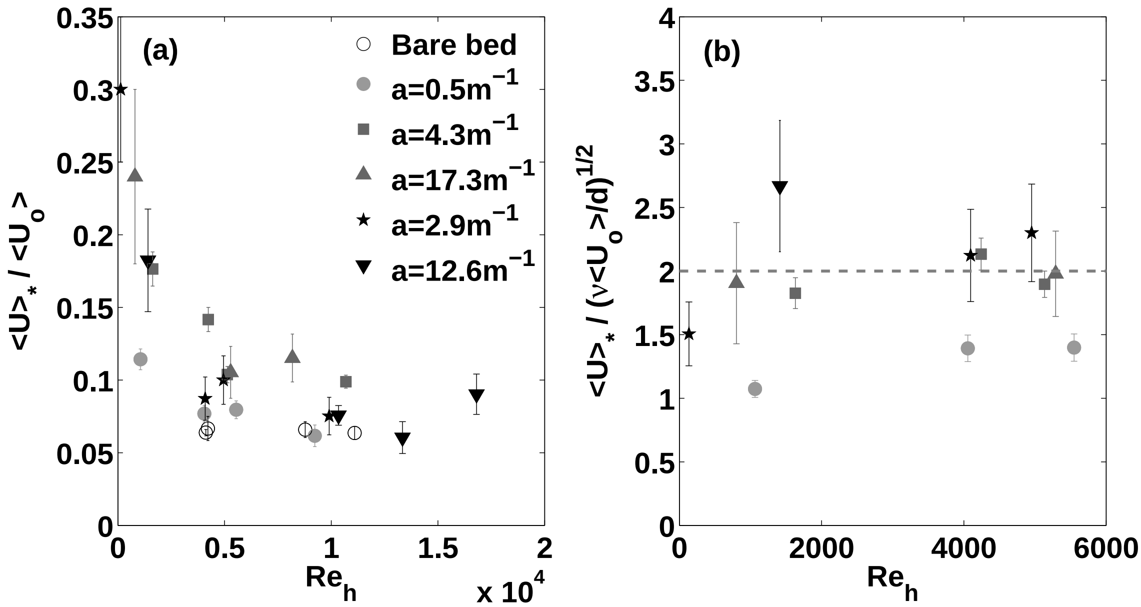

Figure 9. The fitted $\left\langle U\right\rangle_*$ non-dimensionalized by (a) $\left\langle U_o\right\rangle$ and (b) $\sqrt{\left(\nu\left\langle U_o\right\rangle\right)/d}$. The gray circles represent the sparse canopy ($a = 0.5m^{-1}$). In the bare channel with smooth bed (open circles), $\left\langle U\right\rangle_* / \left\langle U_o\right\rangle \approx 0.06$.

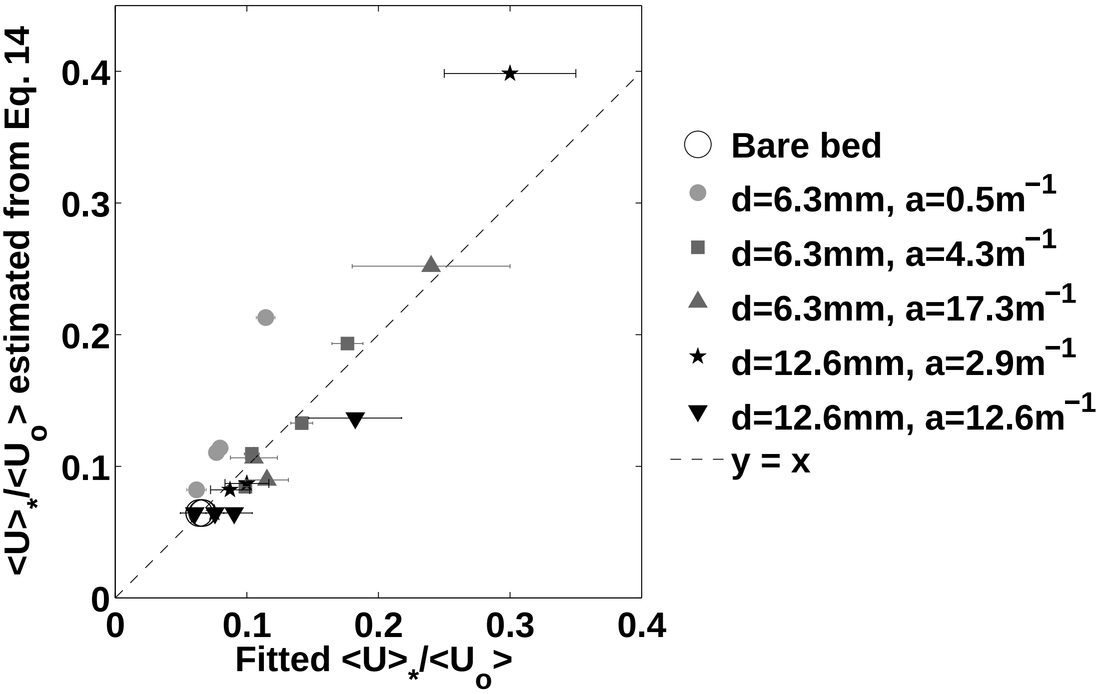

Figure 10. $\langle U \rangle_*$ obtained from Eq.14 normalized by $\langle U_o \rangle$ versus the fitted $\langle U \rangle_*$ normalized by $\langle U_o \rangle$. The open circles represent bare bed value also shown in Fig.9a. The size of the open circle, however, has been enlarged to make the data more distinguishable. The uppermost data point (black pentagram) corresponds to the case with the smallest Re_H as shown in Fig.9a.

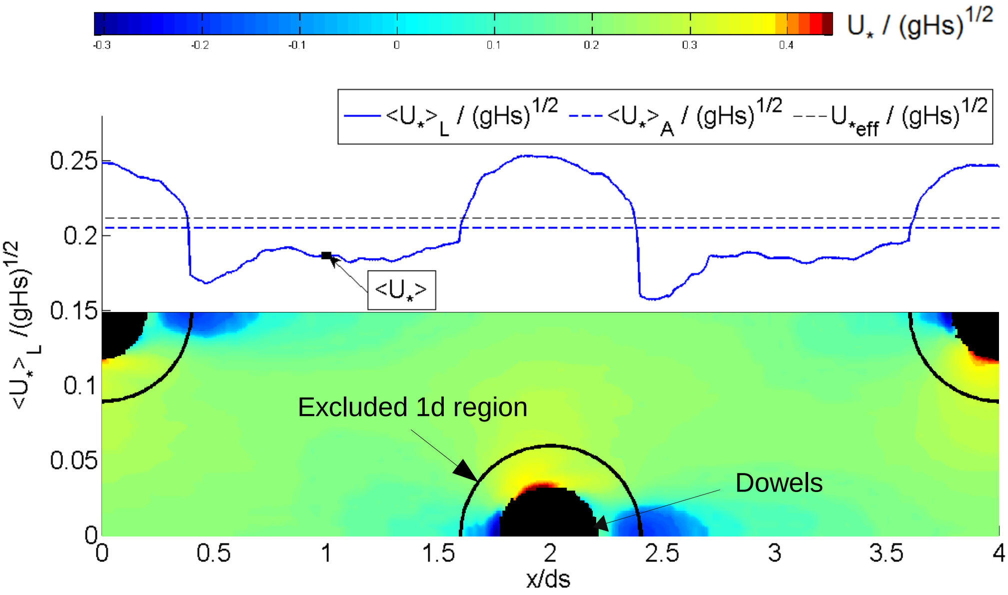

Figure 11. Estimates of bed shear stress normalized by the total stress, $\sqrt{gHs}$. Note that vegetative drag also contributes to the total stress, so that the normalized bed shear stress has an average value less than 1. The color map and color bar is adapted from Fig. 4 of [*Salvador et al.*, 2007]. In their simulation, the flow is from left to right through a staggered array of cylinders with ds (defined in Fig. 1) equal to $2.5d$. U_* is negative if the shear stress on the bed is in $-x$ direction. The depth Reynolds number Re_H is around 3000. The blue curve shows the lateral-average of the simulated $U_*/\sqrt{gHs}$ at each x position excluding 1 diameter region around the dowels. The effective friction velocity U_{*eff} is the black dashed line.

Table 1. Experimental conditions for 24 trials[a]

	Stem diameter $d[m]$	Density $a[m^{-1}]$	Spacing $ds[m]$	Average velocity U $[m/s]$	Water depth H$[m]$	Nb. of profiles (Meas. per profile)
Bare Channel						
Case 1.1	NA	0	NA	0.047	0.083	4 (40)
Case 1.2	NA	0	NA	0.091	0.094	3 (20)
Case 1.3	NA	0	NA	0.036	0.110	4 (39)
Case 1.4	NA	0	NA	0.088	0.124	3 (28)
Emergent vegetation						
Case 2.1	0.0063	0.5	0.056	0.013	0.075	11 (32)
Case 2.2	0.0063	0.5	0.056	0.093	0.098	7 (19)
Case 2.3	0.0063	0.5	0.056	0.050	0.078	9 (28)
Case 2.4	0.0063	0.5	0.056	0.048	0.114	5 (22)
Case 3.1	0.0063	4.3	0.019	0.052	0.097	11 (30)
Case 3.2	0.0063	4.3	0.019	0.083	0.120	7 (21)
Case 3.3	0.0063	4.3	0.019	0.016	0.098	5 (18)
Case 3.4	0.0063	4.3	0.019	0.036	0.117	5 (18)
Case 4.1	0.0063	17.3	0.010	0.054	0.095	7 (23)
Case 4.2	0.0063	17.3	0.010	0.010	0.082	5 (20)
Case 4.3	0.0063	17.3	0.010	0.081	0.104	7 (18)
Case 4.4	0.0063	17.3	0.010	0.047	0.111	5 (17)
Case 5.1	0.0126	2.9	0.033	0.046	0.087	5 (18)
Case 5.2	0.0126	2.9	0.033	0.099	0.098	4 (19)
Case 5.3	0.0126	2.9	0.033	0.041	0.117	4 (16)
Case 5.4	0.0126	2.9	0.033	0.002	0.075	4 (21)
Case 6.1	0.0126	12.6	0.016	0.143	0.117	9 (21)
Case 6.2	0.0126	12.6	0.016	0.098	0.100	5 (18)
Case 6.3	0.0126	12.6	0.016	0.020	0.084	6 (16)
Case 6.4	0.0126	12.6	0.016	0.176	0.074	4 (15)

[a] Case 4.4 has been excluded from our analysis because significant surface waves were observed in this case. The average velocity, U, is calculated as the spatial average of the individual depth-average for each profile. Due to the repeatable pattern of the dowels in y direction, the spatial-average of the depth-averaged velocity along the lateral transect shown in Fig.1 is equal to the volume flow rate per unit cross-sectional area.

Table 2. The friction velocity U_* estimated from three different methods[b]

Bare channel cases	Depth -averaged U$[m/s]$	Total stress method $U_*[m/s]$	Law of the Wall method $U_*[m/s]$	Linear-stress method	
				$U_*[m/s]$	$H_{v+} = \frac{H_v U_*}{\nu}$
Case1.1	0.047	0.0032 ± 0.0001	0.0029 ± 0.0001	0.0030 ± 0.0001	25 ± 4
Case1.2	0.091	0.0057 ± 0.0002	0.0052 ± 0.0003	0.0060 ± 0.0005	19 ± 4
Case1.3	0.036	0.0023 ± 0.0001	0.0023 ± 0.0002	0.0024 ± 0.0003	23 ± 6
Case1.4	0.088	0.0054 ± 0.0002	0.0048 ± 0.0002	0.0056 ± 0.0004	20 ± 3

[b] U_* estimated from three different methods agree within uncertainty. The non-dimensional linear-stress layer height $H_{v+} = 22 \pm 3$ for the bare channel cases we studied.